scientific reports

Check for updates

OPEN

Novel eco-friendly low cost and energy efficient synthesis of $(Nd–Pr–Dy)_2Fe_{14}B$ magnetic powder from monazite concentrate

Syed Kamran Haider[1,2,3], Jin-Young Lee[1], Amol Uttam Pawar[3], Dongsoo Kim[1,2]✉ & Young Soo Kang[3]✉

Syntheses of $Nd_2Fe_{14}B$ magnetic powder by conventional method is a complicated multi-step process, which produces harmful pollutants and consumes a huge amount of energy and resources. Herein we report a simple chemical route for the preparation of $(Nd–Pr)_2Fe_{14}B$ magnetic powder using monazite concentrate as a precursor. Th, U, Sm, and La impurities were removed from monazite leachate by roasting, solvent extraction and leaching the concentrate. Purified leachate consisting of Nd and Pr Chlorides was added to the $FeCl_3$ solution, and the solution produced was co-precipitated with NaOH. RE and Fe hydroxide precipitates were converted to the oxides by annealing at 700 °C. Boric acid and CaH_2 were added in the RE and Fe oxides produced, and this mixture was reduced and diffused to $(Nd–Pr)_2Fe_{14}B$. Magnetic properties of the $(Nd–Pr)_2Fe_{14}B$ produced were enhanced by introducing antiferromagnetic coupling, induced by Dy addition and efficient removal of CaO byproduct through ball milling in ethanol which increased the BH_{max} from 3.9 to 11.45 MGOe. Process reported is energy efficient, environment-friendly, time saving and low-cost.

Rare earth elements (RE) have a wide variety of applications in high-tech products and permanent magnets, hence their demand is increasing rapidly. Monazite is a rich source of various RE, since 70% of the monazite consists of the oxides and phosphates of various RE, mainly of Ce, La, Nd, Pr, and Sm[1–7]. Crystalline phosphate ore in monazite has high chemical and thermal stability, therefore it is quite difficult to extract RE from it. Generally, two chemical methods (acid digestion and leaching process) are commercially applied to obtain the RE from monazite. These processes require high temperature (230 °C) and sulfuric acid to roast the concentrate. Roasting is followed by digestion in which a large quantity of inorganic bases (e.g. NH_4OH, NaOH) hydroxide are used[8,9]. After roasting, digestion, multiple solvent extractions, leaching, and precipitation, RE-oxides are obtained[10]. RE-oxides are reduced to the RE metals by molten salt electrolysis. Reduced RE's are alloyed to the $(Nd\text{-}RE)_2Fe_{14}B$ (RE = Nd, Dy, etc.) after addition of Fe and B. Two major commercialized routes for the production of $Nd_2Fe_{14}B$ magnetic powder are powder metallurgy and melt spinning process. Both of these processes are complicated and need high temperature for alloying steps (e.g. induction melting, strip casting. crushing, Jet milling). Conclusively it takes long time, huge amount of energy and resources to obtain pure RE metals from the monazite and then synthesis of $Nd_2Fe_{14}B$ magnetic powder from them. Among permanent magnets, $Nd_2Fe_{14}B$ hard magnets exhibit the highest magnetic properties such as magnetic remanence and energy density[11–18]. Hence $Nd_2Fe_{14}B$ magnets have huge expanding a market, and it is important to introduce a low-cost, eco-friendly, energy-efficient and time saving method for their production (Fig. S-1).

Herein we report a novel, simple, and convenient chemical method to synthesize $(Nd–Pr)_2Fe_{14}B$ (RE = Nd and Pr) from monazite concentrate. Monazite concentrate was refined by roasting, solvent extraction, and leaching in HCl. Obtained leachate was mixed with $FeCl_3$, then mixture was co-precipitated (to produce RE and Fe hydroxides) and annealed to produce RE and Fe oxides. Boric acid and CaH_2 were added in the RE and Fe oxides and metal oxides were converted to the $(Nd–Pr)_2Fe_{14}B$ by reduction-diffusion (R-D) process. Magnetic properties of the $(Nd–Pr)_2Fe_{14}B$ produced are improved by Dy addition and (removal of CaO through) ball milling in ethanol.

[1]Convergence Research Centre for Development of Mineral Resources, Korea Institute of Geoscience and Mineral Resources, 124, Gwahakro, Yuseonggu, Daejeon 34132, Korea. [2]Powder and Ceramics Division, Korea Institute of Materials Science, 797, Changwondaero, Seongsangu, Changwon, Gyeongnam 51508, Korea. [3]Department of Chemistry, Sogang University, 35, Baekbeomro, Mapogu, Seoul 04107, Korea. ✉email: dskim69@kigam.re.kr; yskang@sogang.ac.kr

Experimental section

Materials. Iron (III) chloride hexahydrate ($FeCl_3{\cdot}6H_2O$), sodium hydroxide (NaOH), boric acid (H_3BO_3), calcium hydride (CaH_2), dysprosium (III) chloride hexahydrate ($DyCl_3{\cdot}6H_2O$), ethyl alcohol (C_2H_5OH), sulfuric acid (H_2SO_4), hexane (C_6H_6) and acetone (CH_3COCH_3) were obtained from Sigma-Aldrich Co.

Primene JM-T and Cyanex 572 were received from Guide chem and CYTEC industries, respectively. All chemicals used in this work were of analytical grade. Korean monazite mineral was provided by convergence research center for development of mineral resources, Korea Institute of geoscience and mineral resources. Visible impurities were removed from the monazite mineral without using any chemical and purified mineral was named monazite concentrate which used as a precursor of Nd and Pr.

Characterization. The concentration of the elements in the monazite leachate was determined by inductively coupled plasma atomic emission spectrometry (ICP-AES, Shimadzu). The morphology, size, and elemental distribution of the intermediate and final product particles were observed with scanning electron microscopy (SEM, MERLIN) and transmission electron microscopy (JEM-2100F TEM, JEOL) operated at 200 kV embedded with energy-dispersive X-ray spectroscopy (EDS). Crystal structure analysis was done with X-ray diffractometer (Rigaku MiniFlex) with Cu-Kα source, with radiation wavelength of 0.15418 nm. For intermediate products, TEM, TEM-EDS, and HRTEM characterizations were performed on JEM-2100F by JEOL Ltd. For TEM analysis, RE and Fe oxide particles were dispersed in ethanol. Magnetic properties were measured by physical property measurement system (PPMS, Evercool II–9T) in the vibrating sample magnetometer mode. JEOL JEM-ARM200F Cs-corrected TEM was used to obtain "High-angle annular dark-field imaging scanning transmission electron microscopy" (HAADF-STEM) and "Low-angle annular dark-field imaging scanning transmission electron microscopy" (LAADF-STEM) images.

Experimental process. Our study is mainly reporting an experimental process; hence the results and discussion section will also explain the experimental process in detail. To avoid the repetition of the information, experimental process has been moved to the supporting information. However, a flow chart of the experimental process is provided as Fig. 1.

Results and discussion

Monazite concentrate used in this work mainly consisted of phosphates and oxides of RE, Th, and U. At first, the concentrate was ground and sieved, as particle size approached 44–500 µm. Almost half of the sample passed through 150 mesh (105 µm) sieve. Sample was mixed with water in such a way that slurry with density of a 100 g/L was formed. The first step was the removal of Th and U from monazite by roasting in (6 N) H_2SO_4. Concentration of both the Th and U was recorded as ~ 0.42 g/L in the slurry. Efficiency of the process was determined by various factors e.g., leaching time, leaching temperature and acid to slurry ratio. Experimental conditions were changed in various experiments and optimum conditions were determined. In optimized process, acid to slurry weight ratio was kept as 1:3 and slurry was roasted at 220 °C for 90 min. Following equation explains the chemical reactions those took place during the roasting step.

$$REPO_4 + 3H_2SO_4 \rightarrow RE_2(SO_4)_3 + 3H_3PO_4$$
$$Th_3(PO_4)_4 + 6H_2SO_4 \rightarrow 3Th(SO_4)_2 + 4H_3PO_4$$
$$U_3(PO_4)_4 + 6H_2SO_4 \rightarrow 3U(SO_4)_2 + 4H_3PO_4$$

To separate U and Th in the form of sulfate salts, Primene JM-T was used. Detail of the solvent extraction process is described in the supporting information.

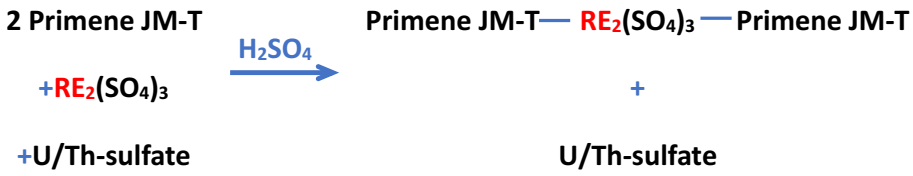

Primene JM-T is a popular reagent used for the solvent extraction of RE. Molecules of the Primene JM-T make organometallic complex with the RE sulfate selectively[19]. During the solvent extraction, sulfates of both the U and Th remained dissolved in the aqueous phase and were separated.

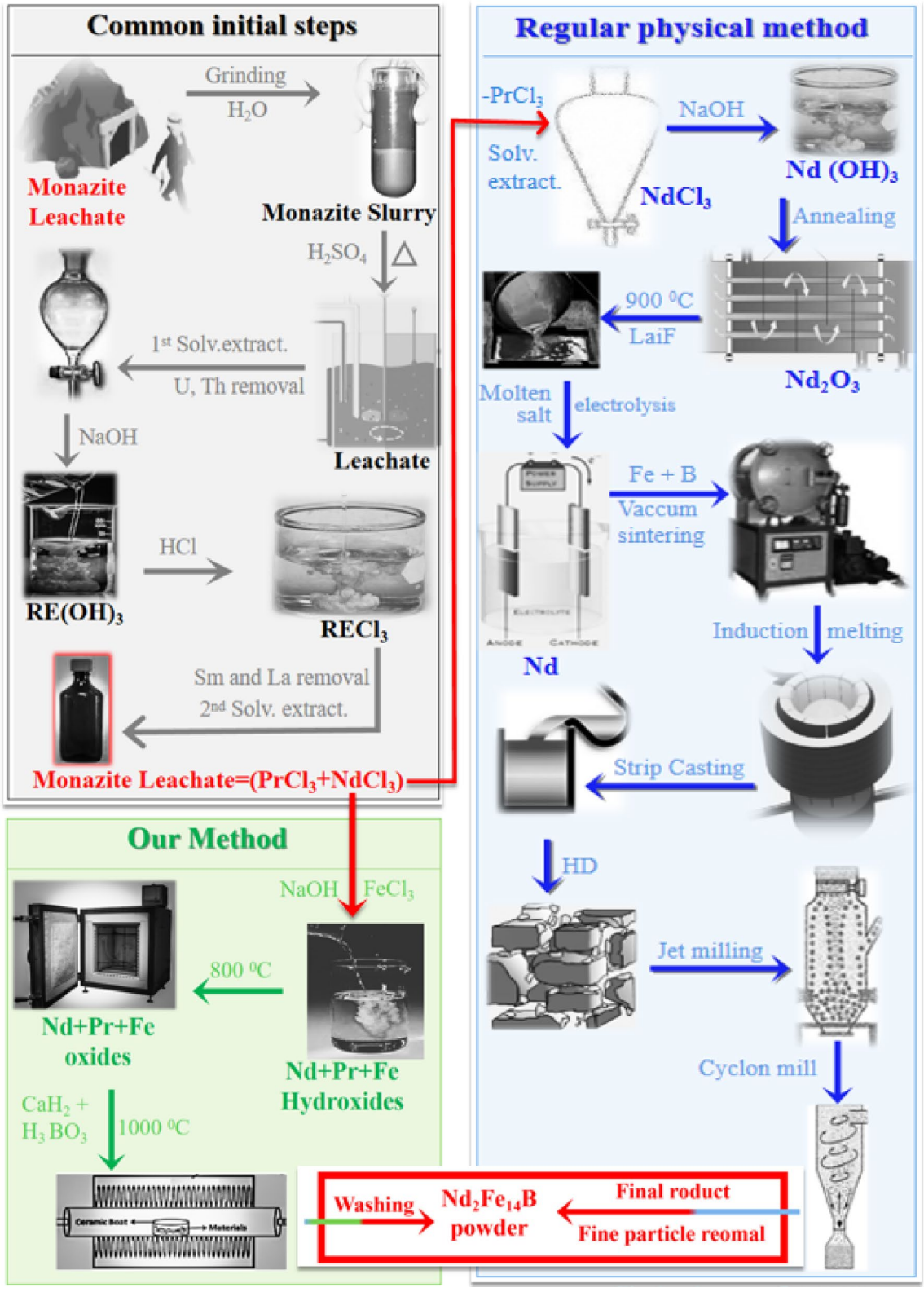

Figure 1. (**a**) Flow chart of our experimental process compared with the regular commercial process.

Elements	Concentration (ppm)
Y	< 1
La	< 1
Ce	< 1
Pr	11,070
Nd	42,480
Sm	174.4
Eu	77.78
Tb	< 1
Dy	70.36
Ho	8.835
Er	< 1
Tm	2.798
Yb	2.622
Lu	< 1
Th	< 1
U	< 1
Gd	212.4

Table 1. Elemental composition of the monazite leachate determined by the ICP-AES analysis.

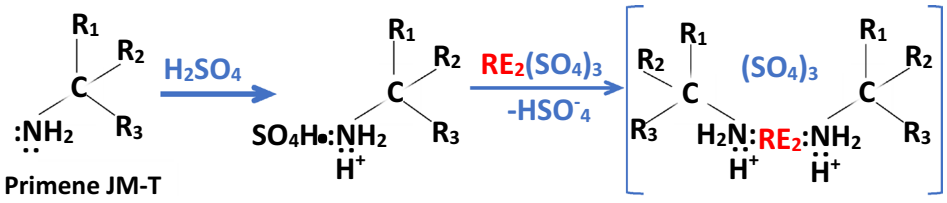

After the extraction of Th and U, in the next step, La and Sm were removed. Solution obtained from the first step was precipitated with (3 M) NaOH until pH value approached 10. $RE(OH)_3$ produced were leached in HCl, hence leachate containing La (12.84 g/L), Pr (1.720 g/L), Nd (5.35 g/L), and Sm (less than 0.01 g/L) was obtained. Sm and La were removed by solvent extraction with Cyanex-572. Detail of the solvent extraction process is described in the supporting information.

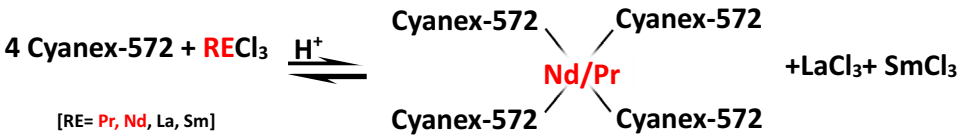

Cyanex-572 is mixture of phosphinic and phosphonic acids[20], which dimerizes and preferentially separates the Nd and Pr from Sm and La. By using Cyanex-572, almost 99.94% of the Sm and La were removed from the leachate.

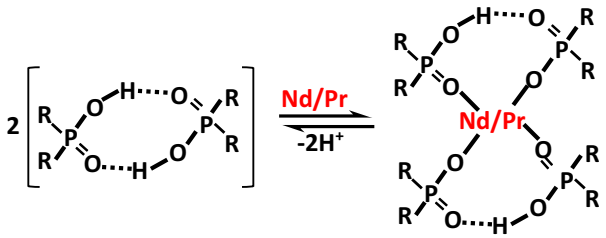

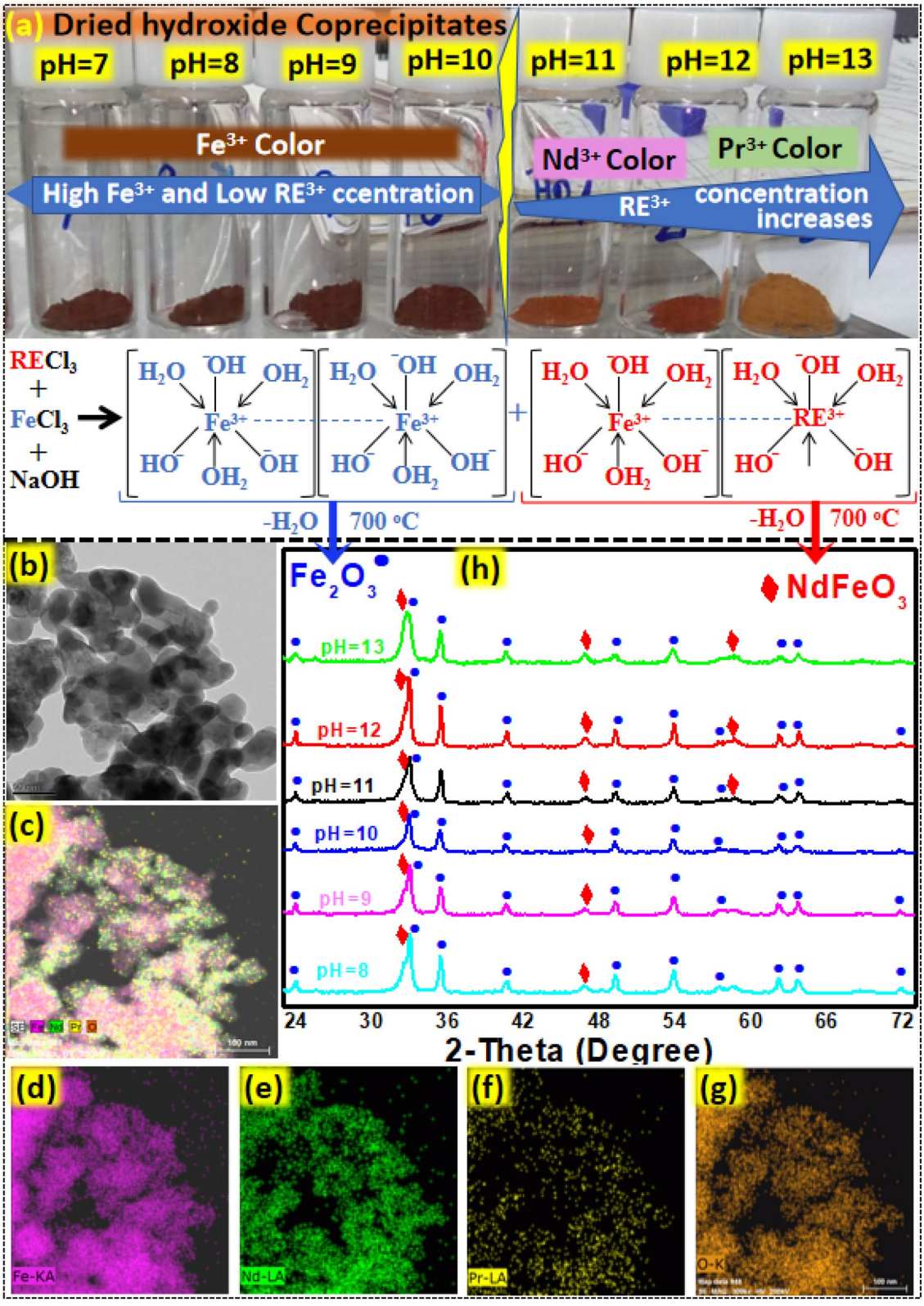

Figure 2. (**a**) Color of the dried hydroxides precipitates precipitated at pH 7–13 (**b**–**g**) TEM and TEM-EDS images of the RE and Fe oxide particles produced at pH 13. (h) XRD patterns for oxides of RE and Fe, produced by annealing their hydroxides.

It was evaluated by ICP-AES analysis that the solution obtained after second solvent extraction, consisted of mixtures of chlorides of various RE (Table 1). This solution was named as monazite leachate. Although leachate consisted of 16 different RE but more than 99% of the leachate comprised of Nd and Pr. Nd:Pr ratio was recorded as 3.83:1.

$FeCl_3$ was added in the monazite leachate solution in such a way that RE:Fe (RE = Nd + Pr) ratio was kept as 15:77. For the synthesis of $(Nd–Pr)_2Fe_{14}B$ by R-D, physical contact between constituent elements in the precursor is very important, because it leads to efficient solid-state diffusion. Hence in this work, co-precipitation was employed for the synthesis of oxide powder. Initial pH of the monazite leachate was 2.64. As NaOH solution was added, red precipitates of Fe $(OH)_3$ were produced and dissolved again immediately. pH of the solution changed slowly until 4 and then after adding very little NaOH, it suddenly raised to the 7.

All RE and Fe Chlorides were converted to hydroxides as presented in the equations below:

$$FeCl_3 + 3NaOH \rightarrow Fe(OH)_3 + 3NaCl$$
$$RECl_3 + 3NaOH \rightarrow RE(OH)_3 + 3NaCl$$

Monazite leachate was co-precipitated at pH 7, 8, 9, 10, 11, 12, and 13 in separate experiments. After co-precipitation at pH 7, 8, 9 and 10, some of the precipitates were suspended in the solution and it took more than 2 h for them to settle down (Fig. S-7). But after co-precipitation at pH 13, it took 25 min for precipitates to settled down (Fig. S-7) completely. When precipitates settled down completely, more than 80% of the by-product (solution of the NaCl and NaOH dissolved in the solution) can be removed just by decanting, without any centrifugation. Hence for the co-precipitation, pH 13 was selected as the optimum pH. In order to remove the co-precipitation by-products (NaCl and NaOH) completely, centrifugation at 4000 rpm for 45 s was carried out.

Fe^{3+} forms highly acidic complexes in monazite leachate. After the addition of NaOH, Fe forms aqua complexes $[Fe(H_2O)_3(OH)_3]$. $[Fe(H_2O)_3(OH)_3]$ is not stable at pH below 7, however, when pH exceeds 7, neutral complexes of Fe precipitate out forming hydroxides. This is the reason that percentage yield increases with increasing the pH. Similarly, $RECl_3$ is converted to $[RE(H_2O)_3(OH)_3]$. By increasing pH more Nd and Pr were precipitated. Colors of Fe^{3+}, Nd^{3+}, and Pr^{3+} are brick red, pink, and light green, respectively. Figure 2a show that precipitation at higher pH produced more $[RE(H_2O)_3(OH)_3]$ as the color of the hydroxide mixture slightly turns brown. Hydroxides of both Fe and RE produced by co-precipitation were amorphous and could not be detected in XRD. $[RE(H_2O)_3(OH)_3]$ and $[Fe(H_2O)_3(OH)_3]$ were converted to the $REFeO_3$ (mainly $(NdFeO_3)$) and Fe_2O_3 by annealing at 700 °C in the presence of air. Oxides produced at various pH were characterized by TEM (Fig. 2 b–g) and XRD (Fig. 2h). By increasing the pH, precipitation of the RE enhanced which could be easily detected around 33 degree in XRD patterns. Precipitation at higher pH reduces the Fe_2O_3 peaks at various points on the XRD patterns, which is more prominent at 72° of 2-theta, where Fe_2O_3 peaks diminished by precipitation at higher at higher pH. Reduction in the Fe_2O_3 peaks and formation of more $REFeO_3$ indicate the increased precipitation of RE at higher pH. TEM analysis revealed that Fe_2O_3 and $NdFeO_3$ had an average particle size of 35 nm (Fig. 2b). TEM–EDX analysis shows the distribution of the RE and Fe oxide particles. (Fig. 2c–g)). Size distribution of the oxide particles is provided in the Fig. S-9.

Co-precipitation at pH 13 gave the highest percentage yield (~99%) of RE and Fe oxides (Fig. S-10), hence oxides produced only at pH 13 were processed further for the next step, R-D. Oxide mixture was mixed with boric acid and CaH_2 and then pressed into pellet form. Pellet was annealed at 1000 °C in the inert environment for the complete R-D of the oxides.

In a separate experiment, $DyCl_3.6H_2O$ was added in monazite solution before co-precipitation. The rest of the experiment was performed the same as the previous experiment. Dy content consequently enhanced the magnetic properties of the final product. Product obtained in this experiment $RE_2Fe_{14}B$ will is labeled as $(Nd–Pr)_{1.5}Dy_{0.5}Fe_{14}B$.

During the R-D, CaO and H_2 were produced as by-product. Produced CaO is helpful to control the particle size by Ostwald ripening during the diffusion and stops the formation of oversized $(Nd–Pr)_2Fe_{14}B$ particles[21]. However, being non-magnetic CaO byproduct reduces the magnetic properties of the magnetic particles. $(Nd–Pr)_2Fe_{14}B$ and, $(Nd–Pr)_{1.5}Dy_{0.5}Fe_{14}B$ were washed with water to remove the CaO. But water reacted with the CaO and formed $Ca(OH)_2$ which is sparingly soluble in water. Consequently, this non-magnetic $Ca(OH)_2$ was left in the $(Nd–Pr)_2Fe_{14}B$ after washing.

For the more efficient removal of the CaO, in another experiment, $(Nd–Pr)_{1.5}Dy_{0.5}Fe_{14}B$ was ball milled in ethanol. CaO removal by ethanol ball milling in this work is different from the study that we reported earlier[22]. In our previous study, milling was performed in a planetary ball milling machine at 300 rpm for 3 h which was quite useful but still had few disadvantages. Milling in the close vessel at high rpm for 3 h increased the temperature of the vessel, which may lead to the partial oxidation of the product. Hence a separate cooling system was attached with the milling apparatus. Secondly, planetary ball milling cannot be used at industrial scale as efficiently as table ball milling. Furthermore, milling at intense conditions as above contaminates the balls and bowl of the milling apparatus and it is not convenient to wash the apparatus after every washing. Hence, in this study common table ball milling apparatus with glass vial (as milling jar) was used, which is much cheaper as compared to the Pulverisette-6 planetary ball mill machine, that was used in the previous study. Most importantly it was found that that table ball mill removed CaO as effectively as the planetary ball mill.

In the current study, 1.5 g of R-D product ($(Nd–Pr)_{1.5}Dy_{0.5}Fe_{14}B$+ CaO) was ground and dispersed in the ethanol (20 ml) in a glass vial. Zirconia balls (70 g) were added to the above mixture and the vial was sealed with the Teflon tap after closing the lid. Ball milling was performed for 3 h at 180 rpm in the open air and then the product obtained was washed with the water thrice to separate the non-magnetic by-products. After the water washing, product was rinsed with acetone twice then stored in the glove box in the inert environment. Final product obtained in this experiment was labeled as $(Nd–Pr)_{1.5}Dy_{0.5}Fe_{14}B$ (BM).

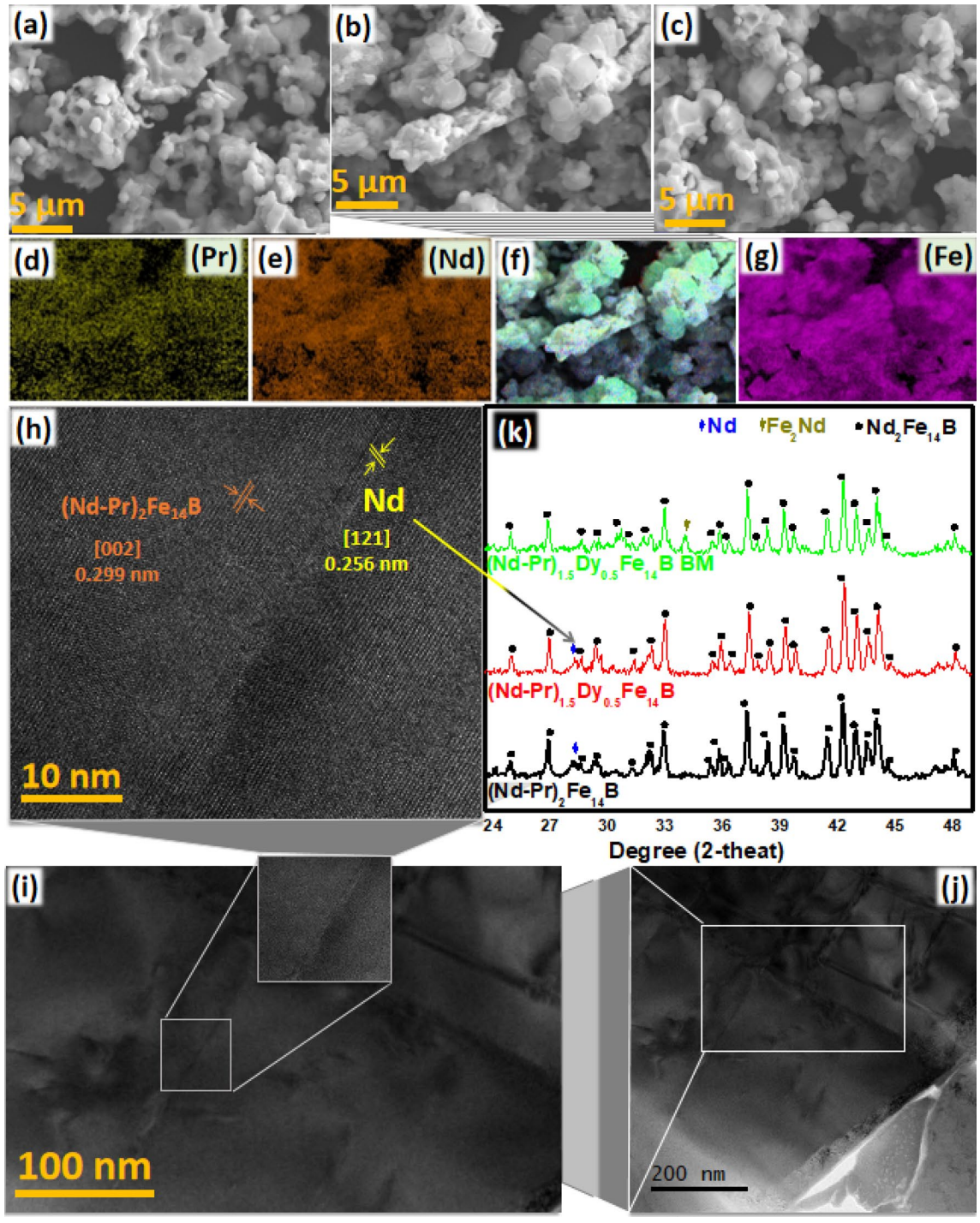

Figure 3. SEM images of (**a**) $(Nd–Pr)_{1.5}Dy_{0.5}Fe_{14}B$ (b) $(Nd–Pr)_2Fe_{14}B$ (**c**) $(Nd–Pr)_{1.5}Dy_{0.5}Fe_{14}B$ (BM). (**d**–**g**) SEM–EDS of images of $(Nd–Pr)_2Fe_{14}B$ (**h**) HAADF-STEM image of $(Nd–Pr)_2Fe_{14}B$ (**i**–**j**) LAADF-STEM image of $(Nd–Pr)_2Fe_{14}B$ B (**k**) XRD patterns for all three products.

Detailed characterization of all three products, $(Nd–Pr)_2Fe_{14}B$, $(Nd–Pr)_{1.5}Dy_{0.5}Fe_{14}B$, and $(Nd–Pr)_{1.5}Dy_{0.5}Fe_{14}B$ (BM) was performed. XRD patterns of all three products described above are very similar. This is because of their very similar crystal structures. However, the ethanol ball milled product did not show any Nd peak (Fig. 3k). Most probably non-magnetic RE phase attached with the magnetic product was removed during ball milling process. From SEM images, average particle size of the $(Nd–Pr)_2Fe_{14}B$, $(Nd–Pr)_{1.5}Dy_{0.5}Fe_{14}B$ and $(Nd–Pr)_{1.5}Dy_{0.5}Fe_{14}B$ (BM) was estimated as 2, 1.5 and 1.3 µm (Fig. 3a–c). SEM–EDS shows the elemental distribution of RE and Fe (Fig. 3d–g) in $(Nd–Pr)_{1.5}Fe_{14}B$. SEM–EDS images provided in the supporting information show the elemental distribution in all three products (Fig. S-11,12,13). This further demonstrates that how after ball milling in ethanol reduced the Ca proportion (Fig. S-11,12,13).

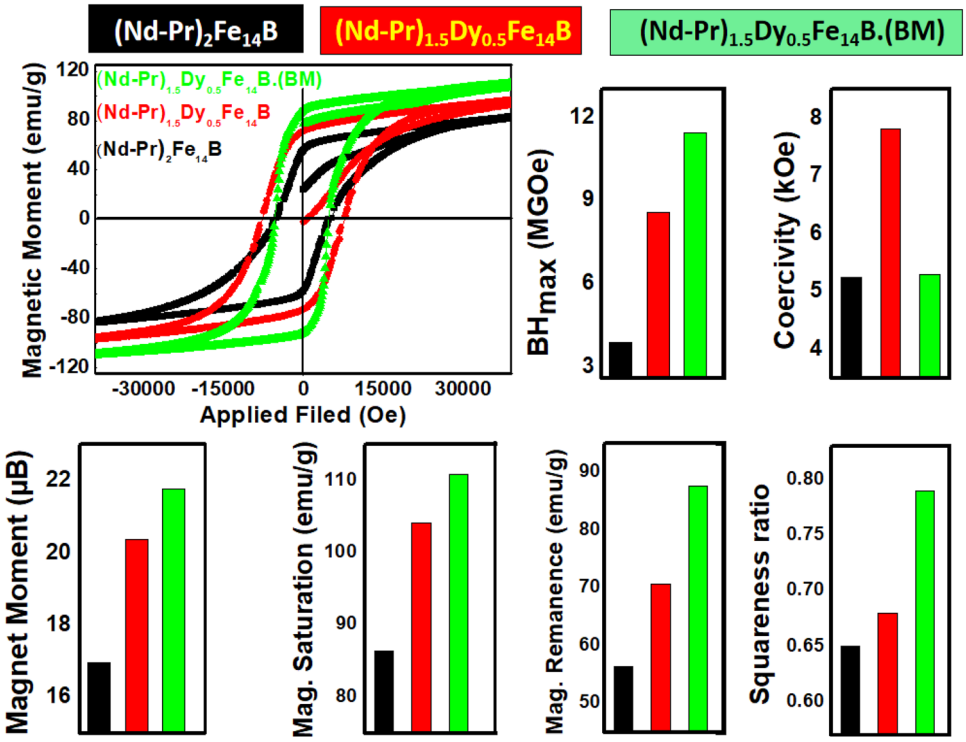

Figure 4. Magnetic hysteresis loop and comparison of magnetic properties of $(Nd–Pr)_2Fe_{14}B$, $(Nd–Pr)_{1.5}Dy_{0.5}Fe_{14}B$ and $(Nd–Pr)_{1.5}Dy_{0.5}Fe_{14}B$ (BM).

To study the micro-structure, LAADF-STEM and HAADF-STEM analysis was performed (Fig. 3h–j). HAADF-STEM image of $(Nd–Pr)_2Fe_{14}B$ shows two mixed crystalline lattice fringes, one is related to (002) plane of $(Nd–Pr)_2Fe_{14}B$ with the d-spacing value of 0.299 nm and another one is related to (121) plane of Nd phase with d- spacing value 0.256 nm, as shown in Fig. 3h. Further confirmation of the Nd phase was monitored by a typical XRD pattern and SEM–EDS images presented in Fig. 3k,d–g, respectively. Additionally, one extra diffraction peak appeared at 2-theta is equal to 28.2° corresponds to the (121) plane of the Nd phase.

There is no evidence that all (~25%) the Dy is substituted in the $Nd_2Fe_{14}B$ crystal lattice. Two main evidence for the Dy substitution in the $Nd_2Fe_{14}B$ come from the XRD and HRTEM. In case of the (~25%) Dy substitution in $Nd_2Fe_{14}B$, XRD peaks are shifted towards right side, because of smaller size of Dy (as compared to the Nd)[21]. In our study, no peak shift was observed and there was no evidence of complete Dy substitution in the HRTEM analysis. However, there is a strong possibility that Dy is partially substituted in the $Nd_2Fe_{14}B$ crystal lattice which is also evident in SEM–EDS. Usually, when $Nd_2Fe_{14}B$ is prepared by the R-D method, added Dy prefers to substitute inside the crystal lattice. However, in our precursors there are 16 RE in the precursors, hence, it is very difficult to know that which RE will substitute inside the lattice and which will remain outside the lattice.

Magnetic properties of all the products together with hysteresis loop are given in Fig. 4. Magnetic moments in (μ_B) are calculated (per formula unit of $(Nd–Pr)_2Fe_{14}B$ from M_s values. Experimentally determined values of magnetic moment (μ_B) in this work are lower than the values predicted by theoretical calculation[22] because experimental conditions conditions are not fixed as theoretical. Theoretical values were calculated assuming the temperature as 5 K (no thermal energy effect), and it was assumed that all particles are single domain and un-oxidized (no washing effect).

Studying the effect of Pr on the of magnetic properties of $(Nd–Pr)_2Fe_{14}B$ is not a straightforward case. Reduction in the Ms and enhancement in the coercivity has been reported after the Pr addition to the $Nd_2Fe_{14}B$[23,24]. But meanwhile contradictory results have also been observed. Zhang et al[25] reported the reduction in squareness ratio (enhancement in Ms value) after Pr addition to the $Nd_2Fe_{14}B$. Imran et al[26] quantitatively measured the enhancement of the magnetic moment (μ_B/formula unit), when 25% Pr was substituted in the $Nd_2Fe_{14}B$ crystal lattice. They reported that overall magnetic moment was enhanced after the Pr substitution (because of the Nd–Pr ferromagnetic coupling).

Main reason for these contradicting results is the position of Pr, in the $(Nd–Pr)_2Fe_{14}B$ based magnetic material. If the Pr is outside the $Nd_2Fe_{14}B$ crystal and found on the grain boundary, it has negligible effect on the magnetic moment. However, in this case it decouples the $Nd_2Fe_{14}B$ grain boundaries effectively. This decoupling enhances the coercivity (and may also reduces the Ms value). If Ms value is reduced this is mainly because of enhancement in the anisotropy energy and coercivity. However if the Pr is substituted in the $(Nd–Pr)_2Fe_{14}B$ crystal lattice overall magnetic moment of the lattice will increase. Enhanced magnetic moment (Ms value) will reduce anisotropy energy and coercivity. During the synthesis of $(Nd–Pr)_2Fe_{14}B$ by R–D method (we also used the R-D method) Pr is usually substituted inside the $Nd_2Fe_{14}B$ crystal. Furthermore, HAADF-STEM image (Fig. 3h) also agrees with

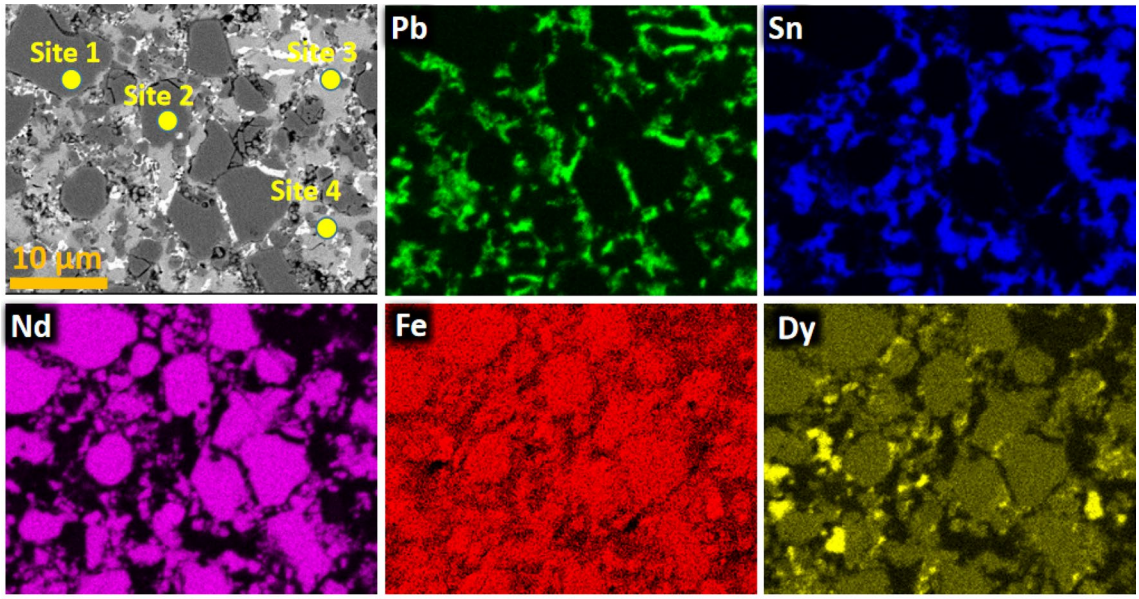

Sites	Fe	Nd	Dy	Pb	Sn
Site 1	85.62	11.78	2.61	-	-
Site 2	85.83	11.61	2.56	-	-
Site 3	23.75	6.42	1.08	10.69	58.06
Site 4	35.32	17.33	47.35	-	-

Figure 5. BSE-SEM and BSE-SEM–EDS images of $(Nd–Pr)_{1.5}Dy_{0.5}Fe_{14}B$.

this statement. That is why in our study, Pr substitution enhanced the Ms value, meanwhile, both the anisotropy energy and the coercivity reduced slightly. The role of Pr on the effect of structural and magnetic properties is further explained in the supporting information.

Dy exhibits almost three times higher magnetic moment as compared to the Nd or Pr and it can affect the magnetic moment of $(Nd–Pr)_{1.5}Dy_{0.5}Fe_{14}B$ in two different ways. If Dy substitutes in the $Nd_2Fe_{14}B$ crystal, it couples antiferro-magnetically with the surrounding elements. However, if Dy is found outside the crystal lattice, it is found as Dy rich phase and there is no antiferro-magnetic coupling involved. Furthermore, paramagnetic behaviour of the Dy can enhance the magnetic moment of the final product. Dy might be oxidized during washing process and produced oxide, which acted as soft magnet. Hence, Dy or Dy_2O_3 phases enhanced the overall magnetic moment of the magnetic particles.

The response of an ideal, homogeneous paramagnetic particles to applied external magnetic field is given by a Langevin function[27]:

$$M = M_s L[\mu\mu_0 H/K_B T] = NL[\mu\mu_0 H/K_B T]$$

where M represents the total magnetization, M_s is the saturation magnetization, μ is magnetic moment of Dy or Dy_2O_3 rich phase, μ_0 is vacuum permeability constant, H is applied field, k_B is Boltzmann's constant, T is temperature, N is density of magnetically-active atoms in the Dy phase, and $L(x) = \coth(x) - 1/x$[27]. Equation above states that magnetization of the Dy or Dy_2O_3 rich phase is directly proportional to the quantity as well as the magnetic moment of the Dy.

Hence, it is proposed that when more Dy is substituted inside the crystal lattice magnetic moment of $(Nd–Pr)_{1.5}Dy_{0.5}Fe_{14}B$ will decrease. On contrary, if more Dy is found outside a crystal lattice overall magnetic moment will increase. Enhanced magnetic moment in $(Nd–Pr)_{1.5}Dy_{0.5}Fe_{14}B$ suggests that there is more Dy outside the crystal lattice as compared to the inside. BSE-SEM and BSE-SEM–EDS images of $(Nd–Pr)_{1.5}Dy_{0.5}Fe_{14}B$ further support this statement (Fig. 5). BSE-SEM analysis was performed by the process reported by Hiader et al.[22] which indicates three regions. One is the main $(Nd–Pr)_{1.5}Dy_{0.5}Fe_{14}B$ phase which is prominent with dark gray color. EDS measurement for site 1 and 2 are taken from that region. Site 3 represents the area which has high concentration of Pb and Sn. These two elements come from the solder. Site 4 indicates the presence of Dy phase, which the Dy phase outside the $(Nd–Pr)_{1.5}Dy_{0.5}Fe_{14}B$ crystal lattice. Conclusively, this Dy increases the magnetic moment of the final product.

Beside the Magnetic Moment Dy addition always increases the anisotropic energy. It is a common observation that when added to $Nd_2Fe_{14}B$, Dy enhances anisotropy energy, M_r and BH_{max}[28–33]. In this work, Dy was also added to increase the anisotropy field and BH_{max}. BH_{max} of the $(Nd–Pr)_{1.5}Dy_{0.5}Fe_{14}B$ approached to 8.56 MGOe

(Fig. 4). CaO produced during R-D process significantly reduces the magnetic properties of the produced magnetic particles[34]. BH_{max} of the $(Nd–Pr)_{1.5}Dy_{0.5}Fe_{14}B$ was improved up to 11.45 MGOe (Fig. 4) by more efficient remal of CaO through ball milling in ethanol.

The addition of Dy increased the coercivity of $(Nd–Pr)_{1.5}Dy_{0.5}Fe_{14}B$ (7.83 kOe) as compared to the $(Nd–Pr)_2Fe_{14}B$ (5.24 kOe). The main reason behind the enhancement in coercivity is the stronger anisotropic field created by Dy. $(Nd–Pr)_{1.5}Dy_{0.5}Fe_{14}B$ had smaller particle size as compared to the $(Nd–Pr)_2Fe_{14}B$ (Fig. 2). It is well-known fact that as particle size gets smaller and approaches the single domain size, coercivity increases. The particle size effect further enhanced the coercivity of $(Nd–Pr)_{1.5}Dy_{0.5}Fe_{14}B$. Another important factor that affected the coercivity was $Ca(OH)_2$ which contaminated the final product when it was washed with water. $Ca(OH)_2$ effectively decoupled the $(Nd–Pr)_2Fe_{14}B$ grains and enhanced coercivity of both $(Nd–Pr)_2Fe_{14}B$ and$(Nd–Pr)_{1.5}Dy_{0.5}Fe_{14}B$. Ethanol ball milling increased the magnetic moment and BH_{max} of $(Nd–Pr)_{1.5}Dy_{0.5}Fe_{14}B$ (BM) but decreased the coercivity value down to 5.31 kOe (Fig. 4).

Among all three products, minimum values of magnetic moment (16.95 μ_B), Mr (56.3 emu/g), and Ms (86.5 emu/g) were recorded for $(Nd–Pr)_2Fe_{14}B$. In contrast, Dy addition enhanced the magnetic moment (20.38 μ_B), Mr (70.6 emu/g), and Ms (104.2 emu/g) values of $(Nd–Pr)_{1.5}Dy_{0.5}Fe_{14}B$.

Removal of non-magnetic $Ca(OH)_2$ phase further increased the magnetic moment. Hence, $(Nd–Pr)_{1.5}Dy_{0.5}Fe_{14}B$ (BM) exhibited the maximum values of magnetic moment (21.67 μ_B), M_r (87.7 emu/g) and M_s (110.8 emu/g). Although Dy addition and $Ca(OH)_2$ removal increased both M_r and M_s values but these factors enhanced the Mr value more as compared to the M_s value. This lead to the enhancement in squareness ratio, which was recorded as 0.65, 0.68 and 0.79 for $(Nd–Pr)_2Fe_{14}B$, $(Nd–Pr)_{1.5}Dy_{0.5}Fe_{14}B$ and $(Nd–Pr)_{1.5}Dy_{0.5}Fe_{14}B$ (BM) respectively.

Conclusion

In a convenient chemical method $(Nd–Pr)_2Fe_{14}B$ particle were synthesized from monazite concentrate. At first Th, Sm, U, and La were separated from monazite by roasting, solvent extraction, and leaching in HCl. Produced monazite leachate mainly consisted of chlorides of Nd and Pr. After addition of $FeCl_3$, Nd and Pr and Fe chlorides were converted to Nd, Pr and Fe oxide by co-precipitation and annealing. Finally, these oxides were reduced and diffused to produce $(Nd–Pr)_2Fe_{14}B$. Pr in the $(Nd–Pr)_2Fe_{14}B$ reduced its energy product because of ferromagnetic coupling with Nd and Fe. Dy addition enhanced anisotropy energy, coercivity and Mr value. Meanwhile, M_r value of the water washed product was reduced because of the presence of the $Ca(OH)_2$, the non-magnetic by-product of the R-D. Ethanol ball milling efficiently removed the CaO, hence BH_{max} was almost tripled (from 3.9 to 11.45 MGOe). Process reported is energy-efficient, environment-friendly, low cost and time-saving.

Received: 2 April 2021; Accepted: 20 September 2021
Published online: 18 October 2021

References

1. Gupta, C. K. & Krishnamurthy, N. Extractive metallurgy of rare earths. *Int. Mater. Rev.* **12**, 197–248. https://doi.org/10.1179/imr.1992.37.1.197 (2013).
2. Hussein, A. E. M. Successive uranium and thorium adsorption from Egyptian monazite by solvent impregnated foam. *J. Radioanal. Nucl. Chem.* **289**, 321–329. https://doi.org/10.1007/s10967-011-1107-x (2011).
3. Abreu, R. D. & Morais, C. A. Purification of rare earth elements from monazite sulphuric acid leach liquor and the production of high-purity ceric oxide. *Miner. Eng.* **23**, 536–540. https://doi.org/10.1016/j.mineng.2010.03.010 (2010).
4. Ilyas, S., Kim, H., Srivastava, R. R. & Choi, S. Cleaner production of rare earth elements from phosphorus-bearing sulfuric acid solution of vein deposit monazite. *J. Clean. Prod.* https://doi.org/10.1016/j.jclepro.2020.123435 (2021).
5. Kumari, A. *et al.* Advanced process to dephosphorize monazite for effective leaching of rare earth metals. *Hydrometallurgy* **187**, 696–703. https://doi.org/10.1016/j.jiec.2014.03.039 (2019).
6. Benitez-Perez, J. M. *et al.* Unraveling the origins and P-T-t evolution of the allochthonous Sobrado unit (Órdenes Complex, NW Spain) using combined U-Pb titanite, monazite and zircon geochronology and rare-earth element. *Geochem. Solid Earth* **11**, 2303–2325. https://doi.org/10.5194/se-11-2303-2020 (2020).
7. Marx, J., Schreiber, A., Zapp, P. & Walachowicz, F. Comparative life cycle assessment of NdFeB permanent magnet production from different rare earth deposits. *ACS Sustain. Chem. Eng.* **5**, 5858–5867. https://doi.org/10.1021/acssuschemeng.7b04165 (2018).
8. Joo, S. H. *et al.* Recovery of molybdenum and rhenium using selective precipitation method from molybdenite roasting dust in alkali leaching solution. *Mater. Trans.* **53**, 2038–2042. https://doi.org/10.2320/matertrans.M2012209 (2012).
9. Kumari, A., Panda, R., Jha, M. K., Kumar, J. R. & Lee, J. Y. Process development to recover rare earth metals from monazite mineral: a review. *Miner. Eng.* **79**, 102–115. https://doi.org/10.1016/j.mineng.2015.05.003 (2015).
10. Sadri, F., Rashchi, F. & Amini, A. Hydrometallurgical digestion and leaching of Iranian monazite concentrate containing rare earth elements Th, Ce, La and Nd. *Int. J. Miner. Process.* **159**, 7–15. https://doi.org/10.1016/j.minpro.2016.12.003 (2017).
11. Brown, D., Ma, B. M. & Chen, Z. J. Developments in the processing and properties of NdFeB-type permanent magnets. *J. Mag. Mag. Mat.* **248**(3), 432–440. https://doi.org/10.1016/S0304-8853(02)00334-7 (2002).
12. Jeong, J. H. *et al.* Chemical synthesis of Nd2Fe14B hard phase magnetic nanoparticles with an enhanced coercivity value: effect of CaH2 amount on the magnetic properties. *New J. Chem.* **40**, 10181–10186. https://doi.org/10.1039/C6NJ02436J (2016).
13. Kim, C. W., Kim, Y. H., Pal, U. & Kang, Y. S. Facile synthesis and magnetic phase transformation of Nd–Fe–B nanoclusters by oxygen bridging. *J. Mater. Chem. C.* **1**, 27. https://doi.org/10.1039/C2TC00083K (2013).
14. Chen, Z., Miller, D. & Herchenroeder, J. High performance nanostructured Nd–Fe–B fine powder prepared by melt spinning and jet milling. *J. Appl. Phys.* **107**, 09A730.10A7303.4. https://doi.org/10.1063/1.3348544 (2010).
15. Ma, X. H. *et al.* Preparation of Nd–Fe–B by nitrate–citrate auto-combustion followed by the reduction–diffusion process. *Nanoscale* **7**, 8016–8022. https://doi.org/10.1039/C5NR01195G (2015).
16. Honshima, M. & Ohashi, K. High-energy NdFeB agnets and their applications. *J. Mat. Engg. Perfo.* **3**(2), 218–222. https://doi.org/10.1007/BF02645846 (1994).
17. Zhong, Y., Chaudhary, V., Tan, X., Parmar, H. & Ramanujan, R. V. High coercivity Dy substituted Nd–Fe–Co–B magnetic nanoparticles produced by mechanochemical processing. *Magn. Magn. Mater.* **475**, 554–562. https://doi.org/10.1016/j.jmmm.2018.08.061 (2019).

18. Rahimi, H., Ghasemi, A., Mozaffarinia, R. & Tavoosi, M. Coercivity enhancement mechanism in Dy-substituted Nd–Fe–B nanoparticles synthesized by sol–gel base method followed by a reduction diffusion process. *J. Magn. Magn. Mater.* **429**, 182–191. https://doi.org/10.1016/j.jmmm.2017.01.041 (2017).
19. Hiskey, J. B. & Copp, R. G. Solvent extraction of yttrium and rare earth elements from copper pregnant leach solutions using Primene JM-T. *Miner. Eng.* **125**, 265–270. https://doi.org/10.1016/j.mineng.2018.06.014 (2018).
20. Syed, K. H., Jin-Young, L., Dongsoo, K. & Kang, Y. S. Eco-friendly facile three-step recycling method of $(Nd–RE)_2Fe_{14}B$ magnet sludge and enhancement of (BH)max by ball milling in ethanol. *ACS Sustain. Chem. Eng.* **8**, 8156–8163. https://doi.org/10.1021/acssuschemeng.0c00584 (2020).
21. Quinn, J. E., Soldenhoff, K. H., Stevens, G. W. & Lengkeek, N. A. Solvent extraction of rare earth elements using phosphonic/phosphinic acid mixtures. *Hydrometal.* **157**, 298–305. https://doi.org/10.1016/j.hydromet.2015.09.005 (2015).
22. Haider, S. K. *et al.* Determination of Dy substitution site in Nd2–xDyxFe14B by HAADF-STEM and illustration of magnetic anisotropy of "g" and "f" sites, before and after substitution. *Sci. Rep.* **11**, 6347. https://doi.org/10.1038/s41598-021-85713-5 (2021).
23. Hirosawa, S., Matsuura, Y., Yamamoto, H., Fujimura, S. & Sagawa, M. Magnetization and magnetic anisotropy of $R_2Fe_{14}B$ measured on single crystals. *J. Appl. Phys.* **59**, 873–879. https://doi.org/10.1063/1.336611 (1986).
24. Rajasekhar, M., Akhtar, D. & Ram, S. The effect of substitution of Nd by Pr on the magnetic properties of melt-spun Nd–Fe–B nanocomposite alloys. *J. Phys. D: Appl. Phys.* **43**, 135004–135010. https://doi.org/10.1088/0022-3727/43/13/135004 (2010).
25. Zhang, W., Zhang, S., Yan, A., Zhang, H. & Shen, B. J. Effect of the substitution of Pr for Nd on microstructure and magnetic properties of nanocomposite $Nd_2Fe_{14}B/\alpha$-Fe magnets. *Mag. Mag. Mat.* **225**(3), 389–393. https://doi.org/10.1016/S0304-8853(01)00015-4 (2001).
26. Khan, I. & Hong, J. Electro. Struc. Site preferences for La and Pr in Nd2Fe14B permanent magnet: a first principles study. *J. Kor. Phys. Soc.* **69**, 1564–1570. https://doi.org/10.3938/jkps.69.1564 (2016).
27. Kai, T. & Ye, T. Magnetic characterization of rare-earth oxide nanoparticles. *Appl. Phys. Lett.* **117**, 122410. https://doi.org/10.1063/5.0023466 (2020).
28. Akiya, T., Kato, H., Sagawa, M. & Koyama, K. Enhancement of coercivity in Al and Cu added Nd–Fe–B sintered magnets by high field annealing. *IOP Conf. Ser.: Mat. Sci. Eng.* https://doi.org/10.1088/1757-8981/1/1/012034 (2009).
29. Yu, N. J., Pan, N. J., Zhang, P. Y. & Ge, H. L. The origin of coercivity enhancement of sintered NdFeB magnets prepared by Dy addition. *J. Magn.* **18**(3), 235–239. https://doi.org/10.4283/JMAG.2013.18.3.235 (2013).
30. Li, W. F., Sepehri-Amin, H., Ohkubo, T., Hase, N. & Hono, K. Distribution of Dy in high-coercivity (Nd, Dy)–Fe–B sintered magnet. *Acta Mater.* **59**, 3061–3069. https://doi.org/10.1016/j.actamat.2011.01.046 (2011).
31. Tan, X., Parmar, X., Zhong, Y., Chaudhary, V. & Ramanujan, R. V. Effect of Dy substitution on the microstructure and magnetic properties of high (BH)max Nd–Dy–Fe–Co–B nanoparticles prepared by microwave processing. *J. Magn. Magn. Mater.* **471**, 278–285. https://doi.org/10.1016/j.jmmm.2018.09.017 (2019).
32. Wenlong, Y. *et al.* Influence of gadolinium on microstructure and magnetic properties of sintered NdGdFeB magnets. *J. Rar. Ear.* **30**, 133–136. https://doi.org/10.1016/S1002-0721(12)60009-X (2012).
33. Zhong, Y., Chaudhary, V., Tana, X., Parmar, H. & Ramanujana, R. V. High coercivity Dy substituted Nd–Fe–Co–B magnetic nanoparticles produced by mechanochemical processing. *J. Magn. Magn. Mater.* **475**, 554–562. https://doi.org/10.1016/j.jmmm.2018.08.061 (2019).
34. Haider, S. K., Ngo, H. M., Kim, D. & Kang, Y. S. Enhancement of anisotropy energy of SmCo5 by ceasing the coupling at 2c sites in the crystal lattice with Cu substitution. *Sci. Rep.* **11**, 10063. https://doi.org/10.1038/s41598-021-89331-z (2021).

Acknowledgements

This work was supported by National Research Council of Science and Technology (NST) grant by the Korea government (MSIT) (No.CRC-15-06-KIGAM). This work was further supported by National Institute of Science and Technology Human Resources Development grant by the Korea government (NST) (No. 202139031.01). Dongsoo Kim also appreciate the support of Leader Project at the Sogang University funded by the Ministry of Science and ICT through the National Research Foundation of Korea (No. 2020R1A3B3079715).

Author contributions

S.K.H. performed experiment did characterization and wrote manuscript. Y.S.K. helped in data interpretation and manuscript writing. D.K. helped in experiment and data interpretation J.Y.L. helped in characterization. A. U. P. helped in the review process and refining the language of the manuscript.

Competing interests

The authors declare no competing interests.

Additional information

Supplementary Information The online version contains supplementary material available at https://doi.org/10.1038/s41598-021-99464-w.

Correspondence and requests for materials should be addressed to D.K. or Y.S.K.

Reprints and permissions information is available at www.nature.com/reprints.

Publisher's note Springer Nature remains neutral with regard to jurisdictional claims in published maps and institutional affiliations.